Approximating Simulated Stochastic Gravitational Wave Background BBHs with Broken Splines and Power Laws

Author: Taylor Knapp[1]
Mentors: Patrick Meyers[2], Arianna Renzini[2]
[1] *Brown University, Providence, RI, U.S.*
[2] *California Institute of Technology, Pasadena, CA, U.S.*
(Dated: August 17, 2022)

The Stochastic Gravitational Wave Background (SGWB) is the combination of assumed isotropic, stationary, unpolarized, and Gaussian sources of gravitational waves. We expect a large contribution of neutron star and black hole binaries to this unresolved signal. Current LIGO detectors are not sensitive enough to the SGWB strain regime but we anticipate future observing runs to have the required sensitivity for the SGWB. The promise of future detectors registering the SGWB requires the introduction of detection and fitting algorithms to understand future observation results. A Reverse Jump Markov Chain Monte Carlo (RJMCMC) algorithm permits us to probe the fitting parameters for SGWB signals via spline and power law fittings. The versatility of the RJMCMC can be applied to the astrophysical case of recovering the energy density spectra based on injected mass distributions and merger rates for binary black hole mergers (BBHs). Accurately fitting the SGWB profiles and parametrizing profiles via spline and broken power laws will aid in identifying various components of the SGWB in data from upcoming LIGO observing runs.

I. INTRODUCTION

Gravitational waves are perturbations of the spacetime manifold expressed by metric tensor $g_{\mu\nu}$ [11]. We are able to detect these fluctuations of space and time as strain, or change in length per unit length. This strain is detected by ground-based interferometers; two of such detectors are LIGO Hanford Observatory (LHO) and LIGO Livingston Observatory (LLO). This style of interferometer involves a laser split in two orthogonal directions and then recombined. These beams reflect off mirrors and coherently return to the source. When a gravitational wave passes, it strains the arms of the detector. This causes the light beams to move out of phase with one another, and so when the beams are recombined the resulting change in the interference pattern is evidence of a passing perturbation of spacetime.

Four primary sources of gravitational waves are coalescing binary systems, pulsars, supernovae, and stochastic gravitational wave backgrounds (SGWB) [3]. We know that coalescing binary systems appear as "chirps". These chirps are the only signals we have detected so far. Pulsars should appear as sine waves due to their periodic emission of gravitational waves. Supernovae are extremely challenging sources to understand since we have yet to detect them, and parametrizing their signal in order to include them in matched filtering searches is extremely unlikely. The fourth source, SGWBs, encompasses the unresolved gravitational wave sources. These unresolved sources include, for example, fluctuations from just after the Big Bang, as well as unresolved astrophysical sources like compact binary coalescences. "Stochastic" refers to a non-deterministic strain signal, either due to the generation process or detector limitations. We cross-correlate data from different detectors to try to detect the SGWB.

Understanding the SGWB will help researchers probe the Universe earlier than electromagnetic signals currently allow [3]. Electromagnetic signals go back to about 400,000 years after the Big Bang, when scattering of particles decreased enough for photons to travel unimpeded. The SGWB could take us as far as 10^{-32} s after the Big Bang because GWs propagate through spacetime without the risk of scattering off particles [12]. For comparison, Planck Time is 5.39×10^{-44} s after the Big Bang. Thus, resolving the primordial background could help paint a clearer picture of the early Universe [11].

Determining a better and more general fit for the SGWB signal will also help us learn about the background itself [3]. As we add more time to our background detection survey, we will be able to resolve more features in the SGWB spectrum. The features in the SGWB spectrum will help us learn about the signals beyond the recognizable, precise events. As Allen [3] mentions, the more we record the signals on multiple detectors simultaneously, the better we will be able to transition the sources of the SGWB from "unresolved" to "resolved", allowing us to understand the astrophysical implications of the parameters we measure and constrain.

Additionally, developing better fits will help bound the stochastic background signal. Narrowing down the frequency ranges where the SGWB signal is present will be helpful to deduce the components of this signal [14]. By fitting parameters to the models we develop during this project, we may be able to better constrain where to turn our attention in our GW searches. Since GW detection is a relatively new scientific development, interpreting as much of the data as we have now will only help us better understand what makes up the SGWB.

Another important application of developing generic fits is recovering parameter profiles given an $\Omega(f)$ energy spectrum. For example, fitting the contributing binary black hole (BBH) merger density rate given the energy profile will help recover specifics about the Universe given

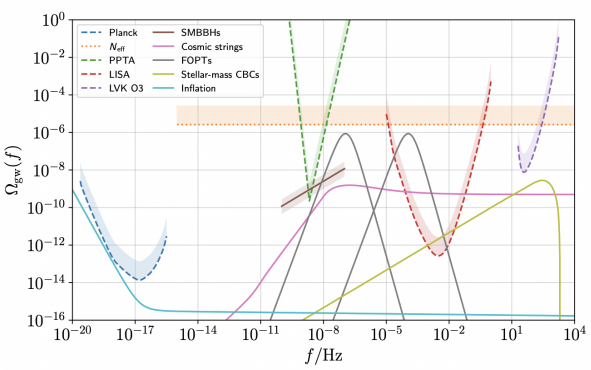

FIG. 1. Various GWB sources, their sensitivity, and their energy density. Figure from Ref [11].

a detected GWB energy background in future observing runs. I will discuss more specifics of this method later in this report, but the astrpohysical ramifications of developing a general fit for SGWB are many and interesting.

II. BACKGROUND

A. SGWB

Most models for a GWB predict a power-law spectrum, which is given by:

$$\Omega_{\rm GW}(f) = \Omega_{\rm ref}\left(\frac{f}{f_{\rm ref}}\right)^{\alpha}, \tag{1}$$

where $\Omega_{\rm GW}(f)$ is the energy density per logarithmic frequency interval used to describe the isotropic stochastic background. This quantity can also be expressed as $\Omega_{\rm GW}(f) = \frac{f}{\rho_c}\frac{d\rho_{\rm GW}}{df}$ where ρ_c is the critical density and $\rho_{\rm GW}$ is energy density of gravitational waves in the infinitesimal frequency interval f to $f + df$ [3]. Fig. 1 provides a visualization for the energy densities expected from different sources across the frequency interval [11]. $\Omega_{\rm ref}$ is the the amplitude at a reference frequency, $f_{\rm ref}$. α is the spectral index. Both $\Omega_{\rm ref}$ and α are constrained using strain data. Right now, we can fit various parameter combinations for different frequency ranges of our spectrum [8].

B. Proposed Fittings

Current alternative functional fittings for the SGWB are as follows:

- Power Law: $\Omega_{\rm GW}(f) = \Omega_{\rm ref}\left(\frac{f}{f_{\rm peak}}\right)^{\alpha}$
- Broken Power law (BPL):
$$\Omega_{\rm GW}(f) = \begin{cases} \Omega_{\rm peak}(\frac{f}{f_{\rm peak}})^{\alpha_1} & \text{for } f \le f_{\rm peak} \\ \Omega_{\rm peak}(\frac{f}{f_{\rm peak}})^{\alpha_2} & \text{for } f > f_{\rm peak} \end{cases}$$
- Smooth BPL:
$\Omega_{\rm GW}(f) = \Omega_{\rm peak}(\frac{f}{f_{\rm peak}})^{\alpha_1}[1 + (\frac{f}{f_{\rm peak}})^{\Delta}]^{(\alpha_2-\alpha_1)/\Delta}$

These models, although simplistic and described by few parameters which require fitting, are not as general and generic as we would like [9]. Alternative functional approaches include spline fitting. Spline fitting utilizes smooth, piece-wise polynomials of different degrees to describe a curve. Parameters come in the form of coefficients of a polynomial expansion:

$$p_j(x) = a_0 + a_1 x + a_2 x^2 + ... + a_n x^n \tag{2}$$

such that the a_i coefficients allow us to fit an n-degree polynomial to the curve segment j. This is advantageous where a single polynomial fit, such as attempting to use a single power law for the entire spectrum, fails. We will start with spline fitting to recover these parameters and their relationships to each other when constructing functional models for our data. In our SGWB analysis, we only require spline fit interpolations up to $n = 3$.

C. RJMCMC Westley Fitting Algorithm

The Westley fitting algorithm utilizes a combination of single power laws and splines to interpolate a fit between an optimized number of knots. Westley is a Reversible Jump Metropolis-Hastings Markov Chain Monte Carlo algorithm [7]. This means that a ratio of likelihoods between points drives the placement of nodes in either the spline or power law fits. The term "Reversible Jump" means that the MCMC can propose adding or removing parameters from a model instead of just probing the existing parameters. First, a guess is made for the placement of the set of nodes along a frequency interval. For now, this guess is made on a uniform prior over the local frequency bin. Next we calculate the likelihood of this node configuration, which is a function of the cross-correlation between detectors and the model we have injected. We are essentially proposing to move a node, interpolating between the nodes to calculate the model, then using that node-motivated model to calculate the likelihood of the data. We then propose to move the amplitude of a node, add another node, or remove a node, and then calculate the likelihood again. If the likelihood of the second node configuration is greater than the likelihood of the first node placement, the second node is kept. Otherwise, we throw out the second node configuration and keep the first node configuration. We repeat this process to form a chain, which should converge at a particular fit to the data.

D. Relevant Equations

An MCMC parameter probe such as Westley relies on probability formulations and statistics. In the following

proposals, a set of equations is used to evaluate the likelihood of the proposal and the Hastings ratio, R. We define the acceptance probability for a node as:

$$P(m'|m) = min\left(1, \frac{p(m')}{p(m)}\frac{p(d|m')}{p(d|m)}\frac{q(m|m')}{q(m'|m)}\right). \quad (3)$$

$p(m)$ is the prior on model m, and $p(d|m)$ is the likelihood of the data given model m. Meanwhile, $q(m|m')$ is the ratio of probability to move from model m to model m' and vice versa. The Hastings ratio, R, is embedded into the acceptance probability and is expressed as:

$$R = \frac{q(m|m')}{q(m'|m)}\frac{p(m')}{p(m)}. \quad (4)$$

The difference between the acceptance probability and the Hastings ratio lies in the probability of the data given the various models that are multiplied into the acceptance probability.

For now, the Hastings ratios are consistently 1. However, in future Gaussian-based updates to the proposals, R will be more complicated, including a Gaussian exponential term. Future work will be deriving and implementing that expression.

E. BBH Energy Spectra in SGWB

We can use Westley to fit a GWB background, but we can also use it to fit population or distributions that contribute to the Ω_{GW} spectrum. This is one of the benefits of developing a generic fitting algorithm. In this section, we introduce the theory behind the BBH energy density spectrum, and discuss how we can use Westley to constrain useful information about the population and distribution of BBHs.

The energy density spectrum for BBH populations given specific populations per redshift and mass probability is:

$$\Omega(f) = \frac{f}{\rho_c}\int dz \frac{\mathcal{R}(z)\langle\frac{dE}{df}|_{f(1+z)}\rangle}{(1+z)H(z)}. \quad (5)$$

$H(z)$ is the Hubble constant as a function of redshift. The $(1+z)$ factor in the denominator of the integral incorporates in the time delay of detecting redshifted objects. The population-averaged energy spectrum with respect to a BBH with object masses m_1 and m_2 is

$$\langle\frac{dE}{df}|_{f(1+z)}\rangle = \int dm_1 dm_2 \frac{dE}{df}(m_1, m_2; f(1+z))p(m_1, m_2) \quad (6)$$

and the merger rate density is:

$$\mathcal{R}(z) = \int dt_d R_*(z_f(z, t_d))F(Z \leq Z_c, z_f(z, t_d))p(t_d), \quad (7)$$

where t_d is the time delay [1]. $F(Z)$ is a function describing the metallicity weighting of the star formation rate, $R_*(z_f)$. TO gain intuition of the metallicity impact on the BBH merger rate, suppose t_d is given a value for the time delayed between detected formation and formation. Then, the overall BBH $\mathcal{R}(z)$ will follow R_* with additional weighting by the metallicity at a given redshift. We weight the star formation rate by the metallicity to inform the model that black holes are more likely to form in low metallicity environments.

To avoid computing a 4D integral, we utilize a matrix multiplication approximation presented by Tom Callister [5]. The computation of this integral occurs in two phases: the precomputation of a grid of mass and redshift values, followed by the calculation of the merger rate density as a function of redshift, z, and time delays, t_d. We may rewrite the population-averaged energy spectrum as a convolution of the radiated energy at every combination of masses, source redshifts and frequencies with the probabilities over the mass grid:

$$\left\{\langle\frac{dE}{df}\rangle\right\}_{f,z} = \sum_{m_1,m_2}\left\{\frac{dE}{df}\right\}_{m_1,m_2,f,z}\{p\}_{m_1,m_2}. \quad (8)$$

The merger rate density becomes a grid of merger redshifts and time delays. The grid of formation redshifts is given as $\{z_f\}_{z,t_d}$. We distinguish between the source and detected reshifts and times due to the time delay of the CBC information reaching our detectors. We additionally utilize the star formation rate, $\{R_*\}_{z,t_d}$, a function we assume the merger rate follows. Finally, we combine these matrices with metallicity weights, $\{F\}_{z,t_d}$, representing the CBC formation as a function of redshift and time. The final expression for the merger rate density becomes:

$$\{\mathcal{R}\}_z = \sum_{t_d}(\{R_*\}_{z,t_d} \times \{F\}_{z,t_d})\{p\}_{t_d}. \quad (9)$$

Using these matrix multiplication approximations, instead of eqn. 5, we write:

$$\Omega(f) = \sum_z \left\{\frac{\mathcal{R}(z)}{(1+z)H(z)}\right\}_z \left\{\langle\frac{dE}{df}\rangle\right\}_{f,z}. \quad (10)$$

The independence of the two terms within the sum allows us to manipulate the merger rate density and energy spectrum independent of each other. In the next section, I will introduce how the various models for $\mathcal{R}(z)$ and $p(m)$ affect the $\Omega(f)$ spectrum.

III. METHODS

A. Mass Probability and Merger Rate Models

Utilizing the matrix multiplication form of $\Omega(f)$ presented by Tom Callister, we may manipulate parame-

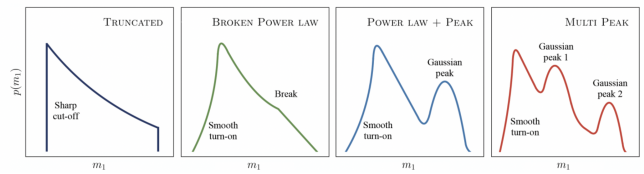

FIG. 2. Mass probability profiles. The assumed mass probability for varied $\mathcal{R}(z)$ is the third profile, power law + peak. The profile gives the probability of having a merger with each respective mass, independent of redshift. Figure from Ref. [2]

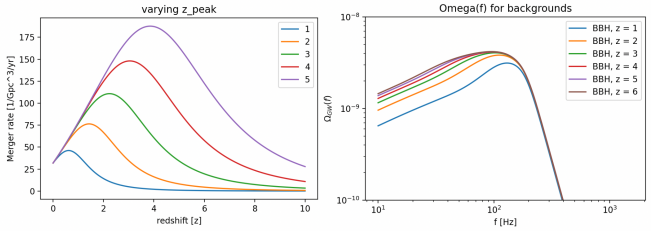

FIG. 3. Variance of only the z_{peak} parameter in $\mathcal{R}(z)$, leaving the spectral indices constant. The left plot shows the merger density rate profile for each z_{peak}. The right plot shows the corresponding $\Omega(f)$ for each varied $\mathcal{R}(z)$.

ters and models of the mass probability distribution and merger rate density. The mass probability distributions predominantly follow those in Abbott, et. al (2021). These four approximate mass probability forms (truncated, broken power law, power law + peak, multi peak) are shown in fig. 3. We will default to the power law + peak profile when varying the merger density rate. The exact model and parameter posteriors that I utilize in my code analysis are also in Abbott, et. al (2021) [2]. For concision, I include the reference but not the extensive parameter posterior figures or tables.

The merger density rate is another story. This profile is assumed to follow the star formation rate relatively closely, as previously described. One common form of the merger rate density that is used, because it is a good analytic description of estimates of the star formation rate, is given by [15]:

$$\mathcal{R}_{BBH}(z) = C(\lambda_1, \lambda_2, z_{peak}) \frac{R_0(1+z)^{\lambda_1}}{1 + \left(\frac{(1+z)}{(1+z_{peak})}\right)^{\lambda_1+\lambda_2}}, \quad (11)$$

where $C(\lambda_1, \lambda_2, z_{peak})$ is the normalization constant allowing $R_{BBH}(0) = R_0$, $R_0 = 31.88\ Gpc^{-3}yr^{-1}$ is the local merger density rate [13], z_{peak} is the location of the highest merge rate density in redshift space, λ_1 is the power law index up until z_{peak}, and λ_2 is the power law index after z_{peak}. Based on the initial value condition, we may manipulate λ_1, λ_2, and z_{peak} for effect on $\Omega(f)$.

IV. RESULTS & DISCUSSION

A. Parameter Variation

The first step of exploring the relationship between $\mathcal{R}(z)$ and $\Omega(f)$ is to vary the parameters of the merger density rate (eqn. 11) and map the effects onto $\Omega(f)$. Increasing z_{peak} alone results in much greater energy at low frequencies, as shown in Fig. 4. We expect this, since increasing z_{peak} alone also increases the area under the $\mathcal{R}(z)$ curve, implying more overall mergers which is effectively proportional to the amount of energy present. However, if we vary the location of the peak while attempting to conserve the area beneath $\mathcal{R}(z)$ as best as possible, we see a different energy density increase effect. Whereas the shift of z alone caused the entire low frequency energy density to increase, horizontally shifting the peak location, as shown in fig. 5, induces an energy density increase at the turnover in the BPL energy density spectrum. This effect agrees with less low-redshift mergers for higher z_{peak}, since those closer BBHs contribute greater to the energy density than high-redshift mergers.

Variation of spectral indices, λ_1 and λ_2, only changes the low frequency energy density before the turnover. This makes sense, since increasing the number of low-redshift BBHs adds energy to the system. In fig. 6, the increase of λ_2 reduces the energy density at low frequencies. This is because cutting off high-redshift mergers and compressing the $\mathcal{R}(z)$ function at low redshifts reduces the overall BBHs allowed in the system, therefore lowering the total energy. Varying the parameters of $\mathcal{R}(z)$ within a reasonable range is a good way for building intuition of the effects of changing the BBH population concentrations at various redshifts on $\Omega(f)$.

B. Pop I/II v. Pop III BBH Spectra

An interesting application of separating and varying merger density rates and mass probabilities is probing the energy density contributions from Pop I/II and Pop III BBHs. There is no formal distinction between Pop I/II and Pop III BBHs, so we assume the general redshift division utilized for Pop I/II v. Pop III stars [10]. To simulate this in our energy density spectrum calculations, we add a Gaussian peak of high merger rate at high redshifts, as if there were a nonnegligible number of BBH mergers at high redshift. We identify this peak in fig. 7. Since we cannot evaluate the Pop I/II and Pop III individually, we evaluate the energy density spectra of the $\mathcal{R}(z)$ with and without the Gaussian peak. The resulting energy density spectrum is shown in fig. 7. Even for a supposed high number of high redshift mergers corresponding to Pop III BBHs, there is still little energy contributed to the GWB from them. The Gaussian peak injected into the merger density rate is exaggerated to induce a noticeable effect on the composite energy density spectrum. As shown in fig. 7, the only nonnegligible

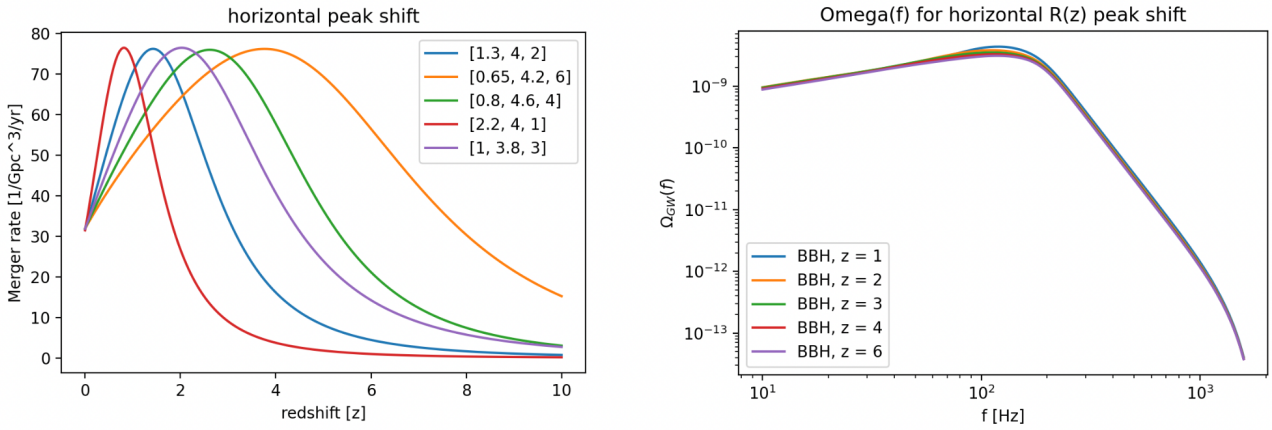

FIG. 4. Horizontal shifting of z_{peak} with corresponding changes in spectral indices λ_1 and λ_2. The left plot shows the merger density rate profile for each z_{peak}. The right plot shows the corresponding $\Omega(f)$ for each varied $\mathcal{R}(z)$.

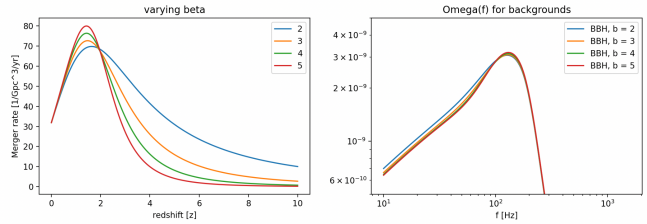

FIG. 5. Variance of only the λ_2 or β parameter in $\mathcal{R}(z)$, leaving the spectral indices constant. The left plot shows the merger density rate profile for each λ_2. The right plot shows the corresponding $\Omega(f)$ for each varied $\mathcal{R}(z)$.

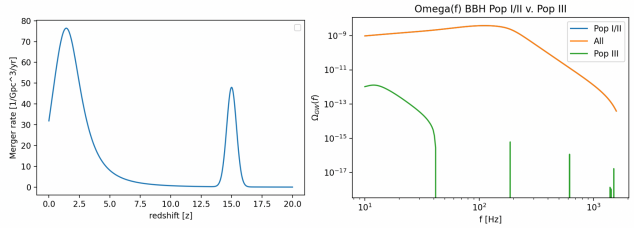

FIG. 6. Plots conveying the Pop I/II BBHs v. Pop III BBHs. The left plot shows the merger density rate with an injected high density of BBHs at high redshift. This Gaussian injection represents an overdensity of Pop III BBHs to observe effects on the energy density spectrum. The right plot shows the very small energy density contribution of Pop III BBHs. Visible energy density spikes in higher frequencies are likely numerical noise.

contribution from Pop III BBHs is at low frequencies. Spikes at higher frequencies are an artifact of numerical noise. Potentially by incorporating a separate mass probability distribution as a result of varying metallicity at high redshift, this profile can be resolved.

C. Strong Lensing Merger Rate

An alternative merger density rate to compare to the form in eqn. 11 is the strong lensing-backed profile [4]:

$$\mathcal{R}(z)_{lens} = N \times S(z) \times M(z). \tag{12}$$

$N \approx 6 \times 10^3$ Gpc^{-3}yr^{-1} is the normalization constant. $S(Z)$, the star formation rate, is given as:

$$S(z) = \frac{(1+z)^{2.7}}{1 + ((1+z)/2.9)^{5.6}} \tag{13}$$

which has visible analog to the parametrized $\mathcal{R}_{BBH}(z)$ in eqn. 11. $M(z)$ is the modulation function defined as:

$$M(z<2) = \frac{2 \times 10^{-4}}{0.1 + z^{1.9}} + e^{-|T(z) - T_{max}|/T_e}. \tag{14}$$

For $M(z \geq 2)$, the modulation function is 1. Lookback time is

$$T(z) = \frac{2}{3H_0}(1+z)^{-1.5} \tag{15}$$

with $T_{max} = T(z=2)$ and estimated parameter $T_e = 0.8$ Gyr. Fig. 8 shows this profile as a function of time. The strong lensing model is driven by the desire to justify so many massive BBHs at redshifts $1 < z < 5$. Gravitational lensing from galaxy clusters and massive intergalactic areas induce lensing on the GWB, magnifying chirp masses. This derived $\mathcal{R}(z)_{lens}$ takes into account this lensing to give a different picture of BBH merger density throughout the Universe.

Utilizing this merger rate density profile instead of the one in eqn. 11 yields an energy density spectrum of magnitude detectable by current observing runs. Strangely, we do not see any artifacts of this profile in our simulations or data. We may vary with some of the parameters

in $\mathcal{R}(z)_{lens}$ to attempt to arrive at a closer profile to our SFR-informed merger rate densities. The T_e parameter controls the changeover from low-z to high-z rates, or when the strong lensing effects on GWB becomes significant. While reducing T_e is helpful for reducing $\Omega_{lens}(f)$, playing with other parameters in the modulation function will be necessary to fully reduce this lensing-informed profile to the expected magnitudes.

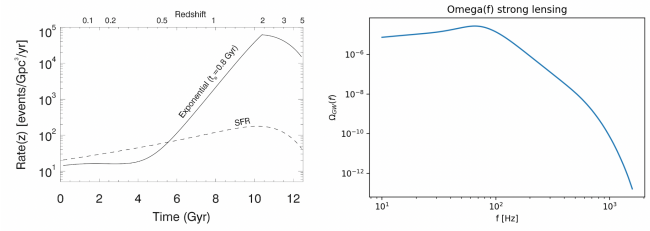

FIG. 7. Strong gravitational lensing informed merger density rate and corresponding $\Omega(f)$ from analysis in Tom Callister's code. Left Fig. from Ref. [4]

V. NEXT STEPS

The next step of this project should take up the remainder of my time in the LIGO SURF. I plan to use the Westley RJMCMC code to see what profiles and parameters can be recovered from a given $\Omega(f)$. Instead of placing the knots for the spline fitting in the data space, $\Omega(f)$, I will place them in the $\mathcal{R}(z)$ space. I will use Tom Callister's code as the model evaluator to see how closely I can fit a merger density rate to the given energy spectrum. That being said, it will be interesting to see what the fitter believes the $\mathcal{R}(z)$ functional form to be. After blind testing, I will hopefully be able to constrain the $\mathcal{R}(z)$ to specific forms to recover parameters from the SFR and strong-lensing informed models. It would be very interesting to be able to recover a model such as $\mathcal{R}(z)$ just given the energy spectrum, which we are able to attain from LIGO observation.

The next step will be to run everything I have run so far with verified constants and parameters, as well as noting the error bars. I have learned so far that ensuring the code and models work is the first step before evaluating the envelope of fits that work for my given model. While I work to use the RJMCMC to recover various merger density rates, I will add in error bars from posteriors.

Overall, it's very exciting to see the application of the Westley RJMCMC to recovering profiles and parameters, which will hopefully help us better understand and extrapolate from the LIGO interferometer data we recieve in future runs.

VI. ACKNOWLEDGEMENTS

I'd like to thank Patrick Meyers and Arianna Renzini for their tremendous support in this project, as well as Tom Callister at UChicago for his astrophysical guidance and code. Also, I'd like to thank the other LIGO Summer Undergraduate Research Fellows (SURFs) for their collaborative spirit and encouraging teamwork. I also gratefully acknowledge the support from the National Science Foundation Research Experience for Undergraduates (NSF REU) program, the California Institute of Technology, and the LIGO Summer Undergraduate Research Fellowship.

[1] Benjamin P Abbott, Richard Abbott, TD Abbott, MR Abernathy, Fausto Acernese, Kendall Ackley, Carl Adams, Thomas Adams, Paolo Addesso, RX Adhikari, et al. Gw150914: Implications for the stochastic gravitational-wave background from binary black holes. Physical review letters, 116(13):131102, 2016.

[2] Rich Abbott, TD Abbott, S Abraham, F Acernese, K Ackley, A Adams, C Adams, RX Adhikari, VB Adya, Christoph Affeldt, et al. Population properties of compact objects from the second ligo–virgo gravitational-wave transient catalog. The Astrophysical journal letters, 913(1):L7, 2021.

[3] Bruce Allen. The stochastic gravity-wave background: sources and detection. In Relativistic Gravitation and Gravitational Radiation, Proceedings of the Les Houches School of Physics, held in Les Houches, Haute Savoie, volume 26, pages 373–418, 1997.

[4] Tom Broadhurst, Jose M Diego, and George F Smoot. A uniform stellar origin for binary black holes revealed by lensing. arXiv preprint arXiv:2202.05861, 2022.

[5] Thomas Callister, Letizia Sammut, Shi Qiu, Ilya Mandel, and Eric Thrane. Limits of astrophysics with gravitational-wave backgrounds. Physical Review X, 6(3):031018, 2016.

[6] Eanna E Flanagan. Sensitivity of the laser interferometer gravitational wave observatory to a stochastic background, and its dependence on the detector orientations. Physical Review D, 48(6):2389, 1993.

[7] Peter J Green. Reversible jump markov chain monte carlo computation and bayesian model determination. Biometrika, 82(4):711–732, 1995.

[8] Vuk Mandic, Eric Thrane, Stefanos Giampanis, and Tania Regimbau. Parameter estimation in searches for the stochastic gravitational-wave background. Physical review letters, 109(17):171102, 2012.

[9] Katarina Martinovic, Patrick M Meyers, Mairi Sakellariadou, and Nelson Christensen. Simultaneous estimation of astrophysical and cosmological stochastic gravitational-wave backgrounds with terrestrial detectors. Physical Review D, 103(4):043023, 2021.

[10] Katarina Martinovic, Carole Perigois, Tania Regimbau, and Mairi Sakellariadou. Footprints of population iii stars in the gravitational-wave background. arXiv preprint arXiv:2109.09779, 2021.

[11] Arianna I Renzini, Boris Goncharov, Alexander C Jenkins, and Patrick M Meyers. Stochastic gravitational-wave backgrounds: Current detection efforts and future prospects. Galaxies, 10(1):34, 2022.

[12] Joseph D Romano, Neil Cornish, et al. Detection methods for stochastic gravitational-wave backgrounds: a unified treatment. Living reviews in relativity, 20(1):1–223, 2017.

[13] Filippo Santoliquido, Michela Mapelli, Nicola Giacobbo, Yann Bouffanais, and M Celeste Artale. The cosmic merger rate density of compact objects: impact of star formation, metallicity, initial mass function, and binary evolution. Monthly Notices of the Royal Astronomical Society, 502(4):4877–4889, feb 2021.

[14] LIGO Scientific, BP Abbott, R Abbott, TD Abbott, S Abraham, F Acernese, K Ackley, C Adams, VB Adya, C Affeldt, et al. Search for the isotropic stochastic background using data from advanced ligo's second observing run. Physical Review D, 100(6):061101, 2019.

[15] LIGO Scientific and Virgo Collaboration. Upper limits on the isotropic gravitational-wave background from advanced ligo and advanced virgo's third observing run. Physical Review D Phys Rev D, 104(2):022004, 2021.

[16] Ashish Sharma and Jan Harms. Searching for cosmological gravitational-wave backgrounds with third-generation detectors in the presence of an astrophysical foreground. Physical Review D, 102(6):063009, 2020.